SCIENCE CHINA Materials ARTICLES

mater.scichina.com link.springer.com

Published online 27 April 2021 | https://doi.org/10.1007/s40843-021-1633-5
Sci China Mater 2021, 64(10): 2613–2623

Exfoliated $FePS_3$ nanosheets for T_1-weighted magnetic resonance imaging-guided near-infrared photothermal therapy *in vivo*

Ying Zhang[1], Hongfang Du[1], Panpan He[1], Chuang Shen[1], Qi Li[1], Yefan Duan[1], Zhouwei Shao[1], Fei Mu[1], Feng Huang[3*], Peiyang Li[2], Pingqi Gao[2], Peng Yu[2*], Zhimin Luo[1*] and Lianhui Wang[1*]

ABSTRACT **Developing bifunctional nanoplatforms integrating advanced biological imaging with high-performance therapeutic functions is interesting for nanoscience and biomedicine. Herein, thin-layered $FePS_3$ nanosheets modified with amine polyethylene glycol ($FePS_3$-PEG) are synthesized by ultrasonicated exfoliation of bulk $FePS_3$ single crystals under Ar atmosphere and *in situ* chemical functionalization with amine PEG. The prepared $FePS_3$-PEG nanosheets give a photothermal conversion efficiency of 22.1% under 808-nm laser and evident T_1 relaxation (r_1 = 2.69 (mmol L^{-1})$^{-1}$ S^{-1}) in external magnetic fields. Biologically experimental results *in vitro* and *in vivo* demonstrate that $FePS_3$-PEG nanosheets have good biocompatibility and exhibit excellent photothermal therapy (PTT) effect under clear T_1-weighted magnetic resonance imaging (MRI). The characteristics of $FePS_3$-PEG nanosheets enable them to be a promising nanomedicine for T_1-weighted MRI-guided near-infrared PTT of cancers.**

Keywords: photothermal therapy, near infrared, T_1 magnetic resonance imaging, thin-layered $FePS_3$ nanosheets, bifunctional nanomedicine

INTRODUCTION

Recently, functional two-dimensional (2D) nanomaterials with superior optical and magnetic properties have been widely studied for biological imaging, diagnosis and therapy [1–7]. 2D transition metal sulfides or oxides, such as MoS_2 [8,9], TaS_2 [10], WS_2 [11], and MnO_2 [12], have attracted more attention because of their unique physicochemical characteristics. For example, MoS_2 nanosheets were used for photothermal ablation of tumors and MnO_2 nanosheets were investigated for magnetic resonance imaging (MRI) [8,9,12,13]. However, few 2D transition metal compounds possess both advanced photothermal properties and T_1-weighted MRI (T_1-MRI) functions.

Ternary layered metal phosphorus trichalcogenides (TLMPT) consisting of three elements exhibit some novel properties because of their chemical and structural diversity as compared with binary layered metal phosphides or metal dichalcogenides [14–16]. Their intrinsic physicochemical characteristics such as optical absorbance, band gap, and magnetism, can be modulated by the choices of elements, which extends the applications of TLMPT in the fields of optoelectronic devices, biological imaging and therapy. Ternary layered iron phosphorus trichalcogenide ($FePS_3$) as a kind of typical TLMPT has special magnetic property and wide-range optical absorbance [17–19]. The unique structure of $FePS_3$ makes it potentially applicable in the electrochemical catalysis and optoelectronic device [19–21]. Nevertheless, there has been no report on the exfoliated thin-layered $FePS_3$ nanosheets for both biological T_1-MRI and near-infrared (NIR) photothermal therapy (PTT) of tumors.

In this work, bulk $FePS_3$ single crystals are ultra-

[1] State Key Laboratory of Organic Electronics and Information Displays & Jiangsu Key Laboratory for Biosensors, Institute of Advanced Materials (IAM), Jiangsu National Synergetic Innovation Center for Advanced Materials (SICAM), College of Electronic and Optical Engineering & College of Microelectronic, Nanjing University of Posts and Telecommunications, Nanjing 210023, China
[2] School of Materials Science and Engineering, State Key Laboratory of Optoelectronic Materials and Technologies, School of Materials, Sun Yat-sen University, Guangzhou 510275, China
[3] Department of Human Anatomy, School of Basic Medical Sciences, Key Laboratory of Brain Aging and Neurodegenerative Diseases of Fujian Province, Fujian Medical University, Fuzhou 350122, China
* Corresponding authors: (emails: huangfengbio@gmail.com (Huang F); yupeng9@mail.sysu.edu.cn (Yu P); iamzmluo@njupt.edu.cn (Luo Z); iamlhwang@njupt.edu.cn (Wang L))

sonically exfoliated into thin-layered $FePS_3$ nanosheets and *in situ* modified with amine polyethylene glycol (PEG-NH_2) for T_1-MRI and NIR PTT (Scheme 1). The PEG-functionalized $FePS_3$ ($FePS_3$-PEG) nanosheets show good photothermal effect under 808-nm laser and evident T_1 relaxation in external magnetic fields besides their good colloidal stability and low biological toxicity. These prominent properties enable $FePS_3$-PEG nanosheets to be a kind of promising bifunctional agents for positive-contrast MRI and NIR PTT of tumors.

EXPERIMENTAL SECTION

Materials

Iron powder (99.95%), red phosphorus powder (99.95%), sulfur (S) powder (99.9%) and dimethyl sulfoxide were purchased from Sigma-Aldrich (USA). Amine polyethylene glycol HCl salt (PEG-NH_2HCl-3K) was purchased from JenKem Technology Co., Ltd. (China). Dulbecco modified Eagle's medium (DMEM), propidium iodide, calcein-acetoxymethyl ester, 3-[4,5-dimethylthiazol-2-yl]-2,5-diphenyl tetrazolium bromide (MTT) and fetal bovine serum (FBS) were purchased from HyClone Boichem Co., Ltd. (China). Human cervical cancer (HeLa) and 4T1 breast cancer (4T1) cells were supplied by KeyGen Biotech Co., Ltd. (China). All aqueous solutions were prepared by using ultrapure water (Millipore, 18.2 MΩ).

Synthesis of $FePS_3$-PEG nanosheets

Few-layered $FePS_3$-PEG nanosheets were prepared by exfoliation of bulk $FePS_3$ single crystals. The bulk $FePS_3$ single crystals were ground into small powders by mortar grinding, and then 50 mg of the $FePS_3$ powders was added into a 25-mL Schlenk tube. The tube was air-evacuated and backfilled with pure Ar. After the vacuum-Ar cycle was repeated for three times, the tube was sealed and protected with Ar. Ar-saturated PEG-NH_2 aqueous solution (33.3 mg mL^{-1}, 15 mL) was added into the tube and sonicated for 9 h. The resultant colloidal suspension was firstly centrifuged at 6000 r min^{-1} for 15 min to remove unexfoliated $FePS_3$ powders and then centrifuged at 10,000 r min^{-1} for 15 min to get $FePS_3$-PEG nanosheets. The $FePS_3$-PEG nanosheets were stored at 4°C for next use.

Characterizations

Scanning electron microscopy (SEM) image and energy dispersive X-ray spectroscopy (EDS) of bulk $FePS_3$ single crystals were characterized by JSM-7600F (JEOL, Japan). Transmission electron microscopy (TEM) and high-resolution TEM (HRTEM) images were taken on HT7700 (Hitachi, Japan) with an acceleration voltage of 100 kV and JEM-2100F (JEOL, Japan) with an acceleration voltage of 200 kV, respectively. X-ray diffraction (XRD) pattern was obtained by using a D8 ADVANCE X-ray diffractometer (Bruker, Germany) with Cu Kα radiation (λ = 1.54178 Å). X-ray photoelectron spectroscopy (XPS) spectra were recorded on a PHI 5000 VersaProbe with Al Kα radiation ($h\nu$ = 1486.6 eV). Raman measurements were carried out on a micro-Raman spectroscopy system (Renishaw, UK) equipped with a 532-nm laser. Photo-

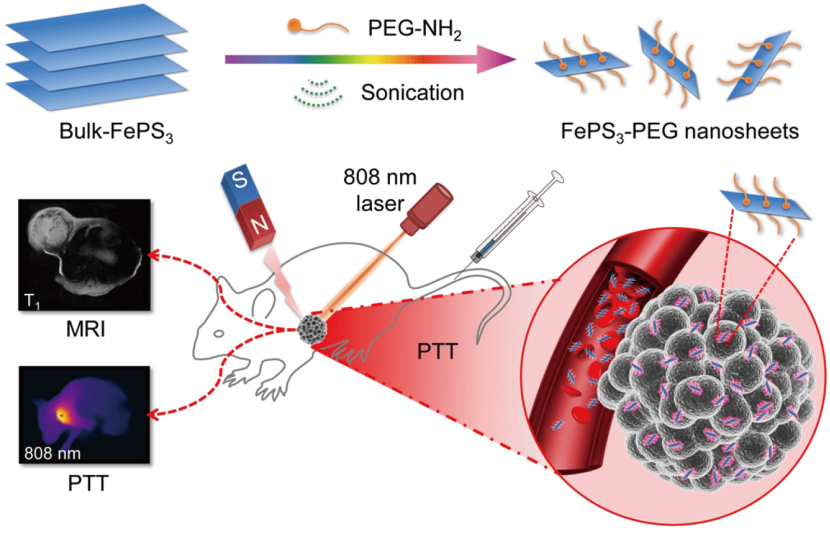

Scheme 1 Schematic presentation of preparing $FePS_3$-PEG nanosheets and their applications for T_1-MRI and NIR PTT *in vivo*.

thermal effect and imaging were measured by a thermal infrared imager (Fotric 225RD). Absorption spectra were recorded by using an ultraviolet-visible-infrared (UV-vis-NIR) spectrophotometer (Shimadzu UV-3600, Japan). The concentration of $FePS_3$-PEG nanosheets was determined by an Optima 5300DV inductively coupled plasma optical emission spectrometer (Perkin Elmer, USA). Size distribution of the $FePS_3$-PEG nanosheets in aqueous suspension was determined by a zeta potential analyzer (Zeta PALS, USA). Fourier transformed infrared spectroscopy (FTIR) spectra of $FePS_3$-PEG nanosheets were measured by an FTIR spectrometer (PE-Spectrum Two, USA).

Photothermal properties of $FePS_3$-PEG nanosheets

$FePS_3$-PEG nanosheets aqueous suspension (200 μL) in a 200-μL centrifuge tube was irradiated by 808-nm laser (0.69 W cm^{-2}) for 10 min to measure their photothermal properties. The temperature change of $FePS_3$-PEG nanosheets in aqueous suspension was monitored by an infrared thermometer. The power density was recorded by a digital power meter. Photothermal heating curves of $FePS_3$-PEG nanosheets with various concentrations (0, 4.1, 8.2, 16.3, 32.7 and 65.3 μg mL^{-1}) were obtained by measuring their temperature changes under 808-nm laser with different power densities. Photothermal conversion efficiency (PCE) of $FePS_3$-PEG nanosheets was evaluated according to their photothermal heating and cooling curves.

Magnetic resonance relaxivity and imaging of $FePS_3$-PEG nanosheets

The longitudinal (T_1) relaxation times and magnetic resonance images of $FePS_3$-PEG nanosheets were acquired using an MRI system (Bruker BioSpin MRI GmbH spect, Nanjing Medical University, China). The r_1 value was calculated by fitting the $1/T_1$ relaxation time (s^{-1}) *versus* the concentration of $FePS_3$-PEG nanosheets. MRI of 4T1 tumors after intravenous injection of $FePS_3$-PEG nanosheets (300 μg mL^{-1}) (dosage = 200 μL of each mice) at different given times (0, 4, 8 and 24 h) was carried out on the same MRI system.

Cytotoxicity assay of $FePS_3$-PEG nanosheets *in vitro*

HeLa cells (10^4 cells per well, 100 μL suspension) were seeded into each well of 96-well plates and incubated for 12 h. After that, the culture medium in wells was removed and then $FePS_3$-PEG nanosheets with different concentrations (0, 10, 20, 30, 40, 50 and 60 μg mL^{-1}) dispersed in DMEM were added into the corresponding wells, respectively. Five wells were set for each sample. After being incubated under 37°C and 5% CO_2 for 24 h, each well was washed with phosphate buffered saline (PBS, pH 7.4, 0.01 mol L^{-1}). MTT (20 μL, 5.0 mg mL^{-1}) dissolved in PBS (pH 7.4, 0.01 mol L^{-1}) was then added into each well, which was incubated under 37°C and 5% CO_2 for an additional 4 h. Dimethyl sulfoxide (200 μL) was added to replace MTT solution in each well for dissolving the formed formazan crystals. The absorbance of cells in each well at 570 nm was measured by a Microplate Spectrophotometer (PowerWave XS2, BIOTEK, US) to evaluate the cytotoxicity of $FePS_3$-PEG nanosheets. Cell viability (%) = (mean absorbance of treatment group/mean absorbance of control) × 100%.

Photothermal therapy *in vitro*

HeLa cells (10^4 cells per well, 100 μL suspension) were seeded into each well of 96-well plates to be incubated for 12 h. After that, culture medium in wells was removed and $FePS_3$-PEG nanosheets with various concentrations (0, 10, 20, 30, 40, 50 and 60 μg mL^{-1}) dispersed in DMEM were added. After being incubated under 37°C and 5% CO_2 for 4 h, each well was irradiated by 808-nm laser (1.0 W cm^{-2}) for 10 min and then incubated for another 12 h. Standard MTT assay was carried out to determine the cell viability. HeLa or 4T1 cells in 96-well plates were imaged by an Olympus FV1000 confocal microscope after being co-stained with propidium iodide and calcein-acetoxymethyl ester. Cytotoxicity and photothermal killing effect of $FePS_3$-PEG nanosheets towards 4T1 cells were carried out by using the similar operations except the incubation conditions of 4T1 cells, which were incubated in Roswell Park Memorial Institute medium (RPMI-1640) containing 10% FBS and 1% penicillin/streptomycin at 37°C under 5% CO_2.

Photothermal imaging and therapy *in vivo*

To test the photothermal imaging and therapeutic effect of $FePS_3$-PEG nanosheets *in vivo*, 4T1 tumor-bearing mice were randomly divided into four groups (5 mice in each group), referred as G1, G2, G3 and G4. Four groups were intravenously injected with 200 μL of saline (G1), $FePS_3$-PEG nanosheets (300 μg mL^{-1}) (G2), saline (G3) and $FePS_3$-PEG nanosheets (300 μg mL^{-1}) (G4), respectively. The mice in G3 and G4 groups were exposed to 808-nm laser (1.0 W cm^{-2}) for 10 min. Photothermal effect and corresponding photothermal imaging of $FePS_3$-PEG nanosheets *in vivo* were measured by using an infrared thermal imaging camera to record the temperature change of tumor sites and their real-time images during

PTT. Tumor volume and body weight of mice were recorded every two days in a period of 3 weeks. Tumor volume = $4\pi/3 \times$ (tumor length/2) $\times$ (tumor width/2)^2. Relative tumor volume (V/V_0) refers to the ratio of the tumor volume at the concerned time after treatment (V) to the initial tumor volume (V_0). For histological analysis, tumor tissue and major organs (heart, liver, spleeny, lung and kidney) of mice harvested from the control and treatment groups were fixed with 4% polyoxymethylene PBS (pH 7.4, 0.01 mol L^{-1}) and embedded in paraffin, which were cut into slices and stained with hematoxylin and eosin (H&E) for imaging. Vein blood was detected in automatic whole blood count (HEMAVET950, USA) for blood routines. 4T1 tumor-bearing or nude mice were purchased from Nanjing OG Pharmaceuticals, Co., Ltd. (China).

All animal experimental procedures were conducted in conformity with institutional guidelines for the animal care and use of laboratory animals, and protocols were approved by the Institutional Ethics Committee for Laboratory Animals of Nanjing Han & Zaenker Cancer Institute (SYXK(SU)2017-0040).

RESULTS AND DISCUSSION

High-quality bulk $FePS_3$ single crystals prepared by a chemical vapor transport (CVT) method (see the details in the Supplementary information) were characterized by SEM. As shown in Fig. S1a, they clearly display layered shapes. EDS characterization and the corresponding analysis in Fig. S1b confirm the compositions of Fe, P and S elements in the bulk $FePS_3$ single crystals. The XRD pattern of bulk $FePS_3$ single crystals (Fig. S2) shows the diffraction peaks at 2θ of 13.9°, 27.8°, 37.7°, 42.5° and 57.6°, which are in good agreement with (001), (002), (201), (003) and (004) planes of the monoclinic structure of $FePS_3$, respectively, according to the standard cards (JCPDS 30-0663 and JCPDS 33-0672) [18–22].

Bulk $FePS_3$ crystals were ground into small powders, which were then directly exfoliated into $FePS_3$ nanosheets under ultrasonication in the Ar-saturated aqueous solution containing PEG-NH_2. The prepared $FePS_3$-PEG nanosheets were characterized by TEM, HRTEM, XRD, Raman and XPS. TEM image (Fig. 1a) reveals the 2D morphology of the product with the average lateral size of less than 200 nm, which is consistent with the result of dynamic light scattering characterization (Fig. S3). EDS mapping images of Fe, P and S elements can be clearly observed from Fig. 1b. The HRTEM image of $FePS_3$-PEG nanosheets (Fig. 1c) shows the lattice spacing of 0.641 nm attributed to (001) plane of $FePS_3$ [20,21,23]. XRD pattern of the prepared $FePS_3$-PEG nanosheets (Fig. 1d) presents the typical diffraction peaks of $FePS_3$ with the monoclinic crystalline structure (JCPDS 30-0663), suggesting the successful synthesis of thin-layered $FePS_3$-PEG nanosheets through our simply ultrasonic exfoliation [18–22]. Raman spectra (Fig. 1e) give the peaks at 160.5, 211.5, 241.8, 273.9, 376.8, 482.0 and 580.8 cm^{-1}. The peak at about 160.5 cm^{-1} corresponds to E_u-type mode of the P_2S_6 unit in $FePS_3$-PEG nanosheets [17,20]. Three peaks at 211.5, 273.9 and 580.8 cm^{-1} are attributed to three E_g-type modes ($E_g^{(1)}$, $E_g^{(2)}$ and $E_g^{(3)}$) of $FePS_3$-PEG nanosheets, and the Raman peaks at 241.8, 376.8 and 482.0 cm^{-1} are attributed to three A_{1g}-type modes ($A_{1g}^{(1)}$, $A_{1g}^{(2)}$ and $A_{1g}^{(3)}$) of $FePS_3$-PEG nanosheets [18,20]. The difference of peak positions at 241.8 and 376.8 cm^{-1} is about 135 cm^{-1}, indicating that the layer number of the

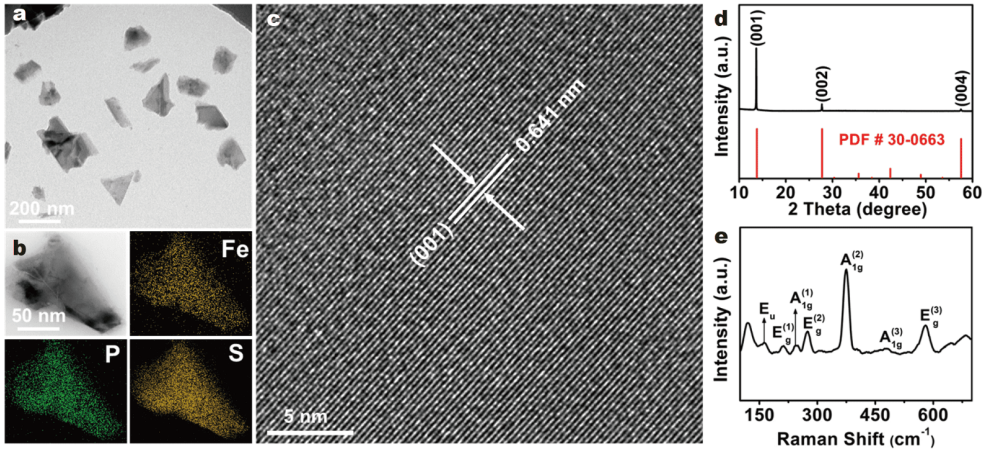

Figure 1 (a) TEM and (b) EDS mapping images of $FePS_3$-PEG nanosheets. (c) HRTEM image of $FePS_3$-PEG nanosheet. The scale bars in (a–c) are 200, 50 and 5 nm, respectively. (d) XRD pattern and (e) Raman spectrum of $FePS_3$-PEG nanosheets.

exfoliated $FePS_3$-PEG nanosheets is about 4 layers [18].

The surface chemical compositions and states of $FePS_3$-PEG nanosheets were confirmed by XPS characterizations. As shown in Fig. 2a, XPS survey spectrum of $FePS_3$-PEG nanosheets presents the binding energies of Fe 2p (720.6 eV), P 2p (132.6 eV), S 2p (162.8 eV) and N 1s (400.2 eV) [20,21,23,24]. The binding energies of Fe $2p_{1/2}$ (722.0 eV) and Fe $2p_{3/2}$ (709.0 eV) of Fe^{2+} can be observed from high-resolution Fe 2p XPS spectrum (Fig. 2b) [20]. The two peaks at 724.1 and 711.2 eV in Fig. 2b are attributable to Fe $2p_{1/2}$ and Fe $2p_{3/2}$ of Fe^{3+}, respectively [20]. High-resolution P 2p XPS spectrum (Fig. 2c) shows two peaks at 132.8 and 132.0 eV belonging to P $2p_{1/2}$ and P $2p_{3/2}$ of P^{4+}, respectively [20,23]. Two peaks at 162.3 and 163.5 eV (Fig. 2d) are assigned to S $2p_{3/2}$ and S $2p_{1/2}$ of S^{2-} [20,23]. The N 1s peak at 400.2 eV corresponding to amine groups (Fig. S4) proves the chemical modification of $FePS_3$ nanosheets with PEG-NH_2 [24]. The FTIR spectrum of $FePS_3$-PEG nanosheets (Fig. S5) shows the peak at 570 cm^{-1} ascribed to $(PS_3)^{2-}$ asymmetric stretching band of $FePS_3$ [25]. The peaks at 1251, 1650, 2915 and 3445 cm^{-1} are ascribed to C–O, C=C, C–H and N–H of PEG-NH_2, respectively [26]. All these characterizations confirm the production of few-layered $FePS_3$ nanosheets functionalized with PEG-NH_2.

The photothermal properties of the prepared $FePS_3$-PEG nanosheets were explored. As shown in Fig. 3a, $FePS_3$-PEG nanosheets have wide-range absorbance from 300 to 900 nm. The absorbance of $FePS_3$-PEG nanosheets increases with their concentrations. The extinction coefficient (ε) of $FePS_3$-PEG nanosheets at the wavelength of 808 nm is estimated to be 5.1 L g^{-1} cm^{-1} (Fig. 3b) according to Lambert-Beer's law [27], which is higher than those of previously reported Au nanorods (3.9 L g^{-1} cm^{-1}) [28] and nanosized graphene oxides (3.6 L g^{-1} cm^{-1}) [29]. Photothermal heating curves in Fig. 3c show that the temperatures of $FePS_3$-PEG nanosheets increase with their concentrations under the same irradiated time of 808-nm laser. Photothermal images of $FePS_3$-PEG nanosheets with various concentrations (0, 4.1, 8.2, 16.3, 32.7 and 65.3 μg mL^{-1}) are presented in Fig. S6a. The rate of photothermal temperature evolution for $FePS_3$-PEG nanosheets is dependent on the power densities of 808-nm laser (Fig. S6b). The temperature-evolution curve

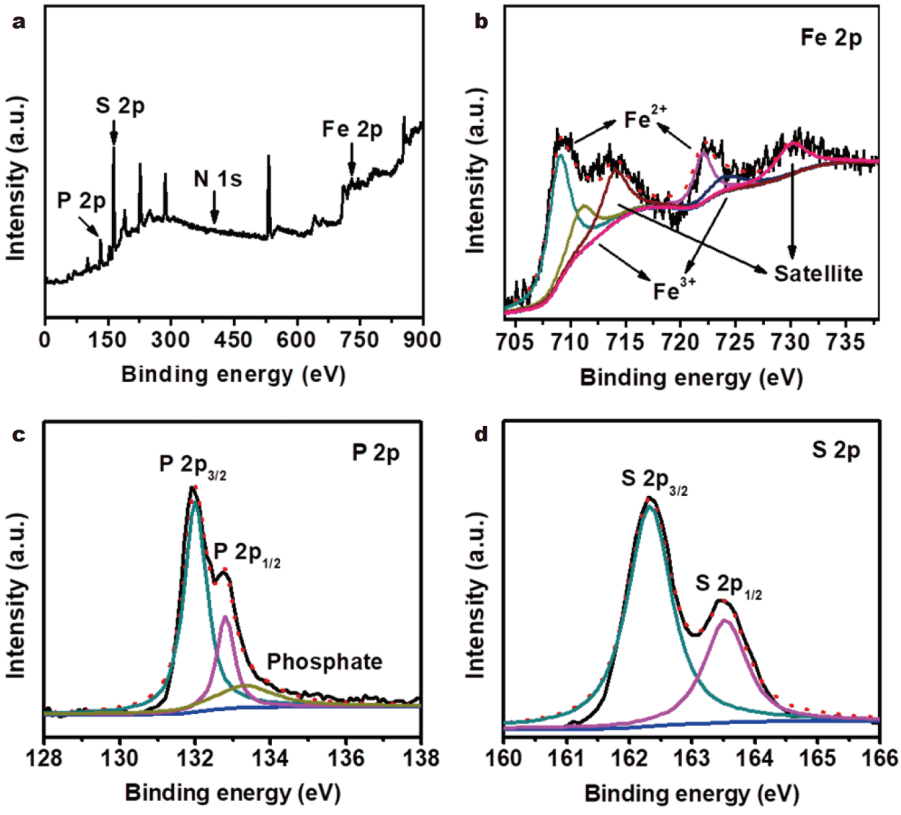

Figure 2 (a) XPS survey spectrum of $FePS_3$-PEG nanosheets. High-resolution XPS spectra of (b) Fe 2p, (c) P 2p and (d) S 2p for $FePS_3$-PEG nanosheets.

of $FePS_3$-PEG nanosheets (65.3 μg mL^{-1}) during heating and cooling (Fig. 3c, d) displays that the temperature of $FePS_3$-PEG nanosheets (65.3 μg mL^{-1}) increases by 37°C after being irradiated by 808-nm laser (0.69 W cm^{-2}) for 5 min, while that of deionized water only increases by 3.8°C (Fig. 3c). PCE of $FePS_3$-PEG nanosheets was calculated to be 22.1% at the wavelength of 808 nm (Fig. 3e) according to the reported method [27,30], which is slightly higher than that of Au nanorod (21%), a representative photothermal agent [31]. These results demonstrate the rapid and efficient conversion of NIR optical energy into thermal energy by $FePS_3$-PEG nanosheets. The photothermal stability of $FePS_3$-PEG nanosheets was also investigated. As shown in Fig. 3f, the photothermal performance of $FePS_3$-PEG nanosheets shows no evident deterioration after five repeated heating and cooling operations, indicating the long-term durability of $FePS_3$-PEG nanosheets as a photothermal agent. In order to apply $FePS_3$-PEG nanosheets *in vitro* and *in vivo*, their chemical stabilities were also studied. As shown in Fig. S7, there are almost no changes for $FePS_3$-PEG nanosheets kept in deionized water, PBS (pH 7.4, 0.01 mol L^{-1}), physiological buffered saline (PBS + 0.9% NaCl) and DMEM for 5 d.

Cytotoxicity of $FePS_3$-PEG nanosheets *in vitro* was tested by MTT assay using HeLa and 4T1 cells as models. It can be observed from Fig. 4a, b that the viabilities of both HeLa and 4T1 cells are still more than 80%, even though the concentration of $FePS_3$-PEG nanosheets is over 60 μg mL^{-1}. To evaluate the PTT effect of $FePS_3$-PEG nanosheets *in vitro*, HeLa and 4T1 cells were incubated with $FePS_3$-PEG nanosheets (0, 10, 20, 30, 40, 50 and 60 μg mL^{-1}) and subsequently exposed to 808-nm laser for 5 min. The viabilities of both HeLa and 4T1 cells incubated with $FePS_3$-PEG nanosheets decrease sharply after the treatment of 808-nm laser (Fig. 4a, b), indicating the strong photothermal killing effect of $FePS_3$-PEG nanosheets. Fluorescence confocal imaging of treated HeLa and 4T1 cells further confirms the photothermal killing effect of $FePS_3$-PEG nanosheets *in vitro*. As shown in Fig. 4c, d, most of HeLa and 4T1 cells can be efficiently killed after being incubated with $FePS_3$-PEG nanosheets and then treated with 808-nm laser, while most of HeLa and 4T1 cells incubated with $FePS_3$-PEG nanosheets but no treatment by 808-nm laser still keep alive.

Bulk $FePS_3$ single crystals as a novel class of magnetic 2D materials can be exfoliated to produce thin-layered $FePS_3$ nanosheets with small sizes for biological and medical applications. As observed from the measurements of longitudinal (T_1) relaxation time of protons in $FePS_3$-PEG nanosheets aqueous suspension under external magnetic fields (Fig. 5a), the $FePS_3$-PEG

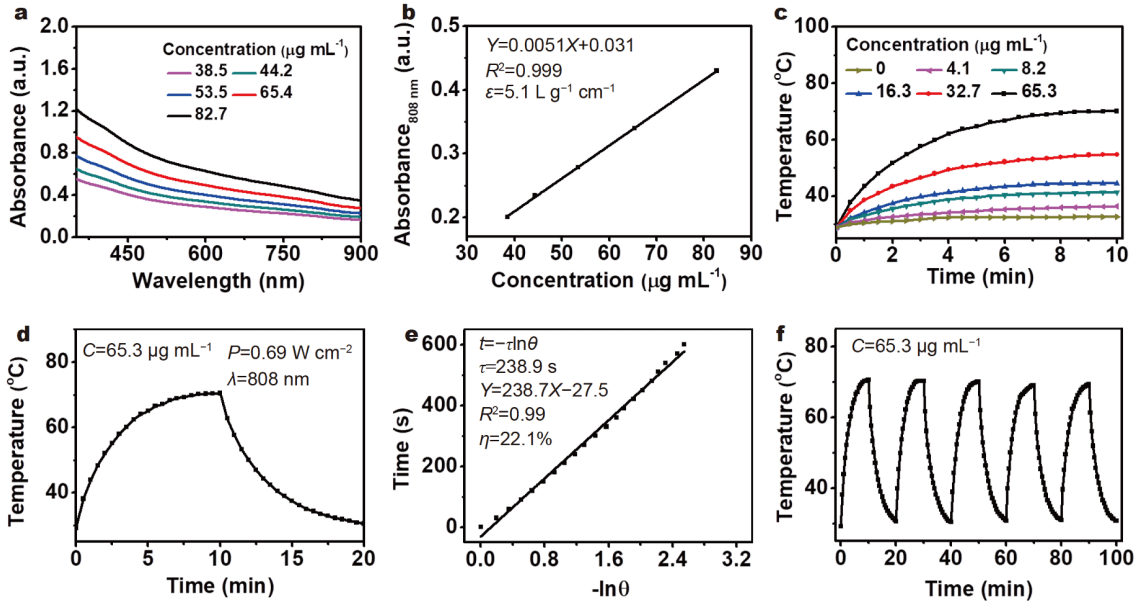

Figure 3 (a) Absorption spectra of $FePS_3$-PEG nanosheets (38.5, 44.2, 53.5, 65.4 and 82.7 μg mL^{-1}). (b) Normalized absorbance of $FePS_3$-PEG nanosheets (38.5, 44.2, 53.5, 65.4 and 82.7 μg mL^{-1}) at the absorption wavelength of 808 nm. (c) Photothermal heating curves of $FePS_3$-PEG nanosheets with various concentrations (0, 4.1, 8.2, 16.3, 32.7 and 65.3 μg mL^{-1}) under 808-nm laser. (d) Temperature evolution of $FePS_3$-PEG nanosheets (65.3 μg mL^{-1}) exposed to 808-nm laser during heating and cooling. (e) Thermal equilibrium time constant (τ) and PCE (η) of $FePS_3$-PEG nanosheets. (f) Photothermal stability of $FePS_3$-PEG nanosheets during repeated heating and cooling operations.

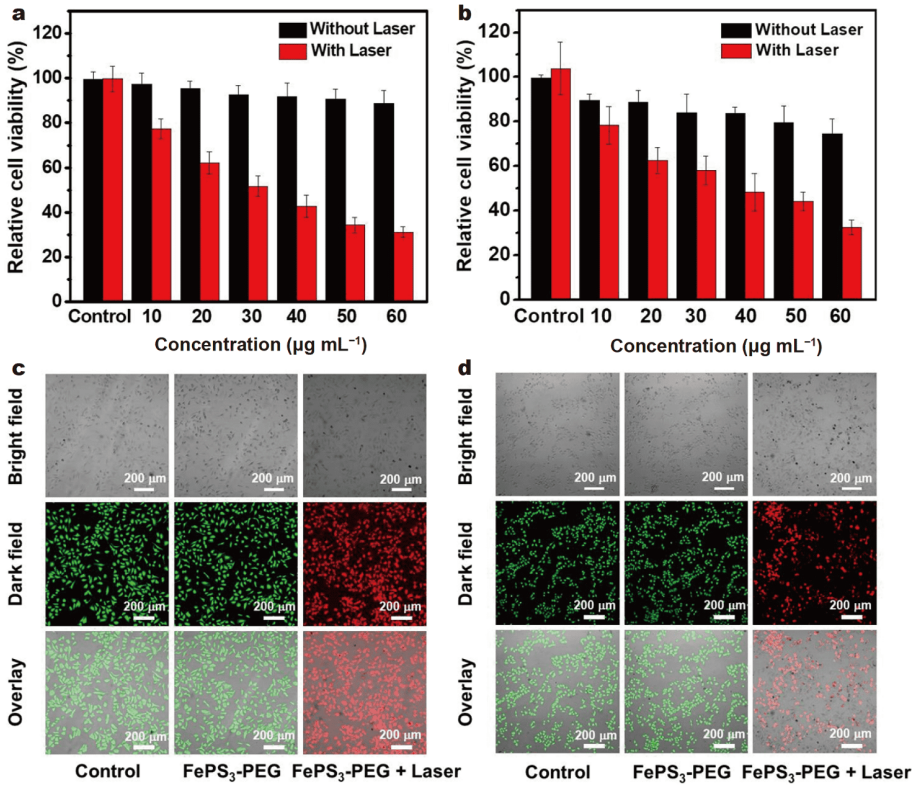

Figure 4 Viabilities of (a) HeLa and (b) 4T1 cells incubated with $FePS_3$-PEG nanosheets and then treated without or with 808-nm laser. Fluorescence confocal imaging of (c) HeLa and (d) 4T1 cells incubated with $FePS_3$-PEG nanosheets and then treated without or with 808-nm laser. HeLa and 4T1 cells were co-stained with propidium iodide (red) and calcein-acetoxymethyl ester (green) for fluorescence confocal imaging. Power density of 808-nm laser: 1.0 W cm^{-2}.

nanosheets exhibit the evident T_1 relaxivity (r_1 = 2.69 $(mmol\ L^{-1})^{-1}\ S^{-1}$). The r_1 value is higher than those of reported tannic acid-Fe@bovine serum albumin complex (1.1 $(mmol\ L^{-1})^{-1}\ S^{-1}$) [32], MnO nanoparticles (0.37 $(mmol\ L^{-1})^{-1}\ S^{-1}$) [33], Fe_3O_4 nanoparticles (1.1 $(mmol\ L^{-1})^{-1}\ S^{-1}$) [34], Fe_3O_4@MnO nanoparticles (1.3 $(mmol\ L^{-1})^{-1}\ S^{-1}$) [34], zwitterion-coated ultrasmall iron oxide nanoparticles (1.5 $(mmol\ L^{-1})^{-1}\ S^{-1}$) [35], extremely small iron oxide (0.68 $(mmol\ L^{-1})^{-1}\ S^{-1}$) [36], and is close to commercial ferumoxytol (3.1 $(mmol\ L^{-1})^{-1}\ S^{-1}$) [35] and gadolinium-diethylenetriamine pentaacetic acid (Gd-DTPA) (3.1 $(mmol\ L^{-1})^{-1}\ S^{-1}$) [37]. It suggests that $FePS_3$-PEG nanosheets are promising as a T_1-MRI agent of cancers. As shown in Fig. 5b and Fig. S8, after intravenous injection of $FePS_3$-PEG nanosheets for different times (0, 4, 8, 24 h), the accumulation of $FePS_3$-PEG nanosheets on the tumor region results in clear contrast-enhanced T_1-MRI of the tumor site. The high-contrast T_1-MRI of $FePS_3$-PEG nanosheets makes them potentially applied to guide PTT of tumors.

Based on their NIR photothermal characteristics and MRI performance *in vivo*, $FePS_3$-PEG nanosheets were further studied for MRI-guided PTT of 4T1 tumors. After 4T1 tumor-bearing mouse was intravenously injected with $FePS_3$-PEG nanosheets and the tumor region was exposed to 808-nm laser, the temperature of tumor region increased rapidly from 36.1 to 48.0°C in less than 3 min (Fig. 5c, G4: green line). In contrast, the temperature of tumor region displays almost no changes after intravenous injection of saline (Fig. 5c, G1: black line) or $FePS_3$-PEG nanosheets without the treatment by 808-nm laser (Fig. 5c, G2: red line). The temperature of tumors treated directly by 808-nm laser without $FePS_3$-PEG nanosheets only increases by 4°C (Fig. 5c, G3: blue line). These photothermal measurements demonstrate the strong photothermal effect of $FePS_3$-PEG nanosheets *in vivo*, which is also confirmed by their corresponding photothermal imaging of 4T1 tumor-bearing mice (Fig. 5d). H&E staining of tumor tissues obtained from G1, G2 and G3 (Fig. 6a–c) shows no significant tumor

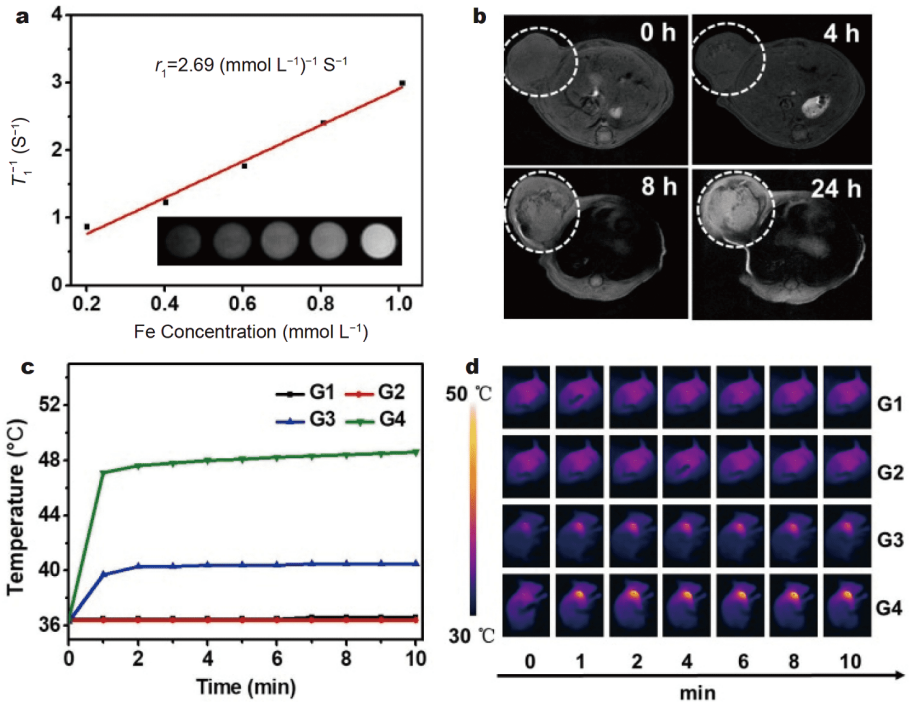

Figure 5 (a) Magnetic resonance measurements and imaging (inset) of $FePS_3$-PEG nanosheets. (b) MRI of the tumor sites after intravenous injection of $FePS_3$-PEG nanosheets for different times (0, 4, 8, 24 h). (c) Temperature evolution of the tumor sites exposed to 808-nm laser after intravenous injection of $FePS_3$-PEG nanosheets for 12 h. (d) Photothermal imaging of 4T1 tumor-bearing mice. G1: Saline; G2: $FePS_3$-PEG nanosheets; G3: Saline + 808-nm laser; G4: $FePS_3$-PEG nanosheets + 808-nm laser. Power density of 808-nm laser: 1.0 W cm^{-2}. Concentration of $FePS_3$-PEG nanosheets: 300 μg mL^{-1}.

tissue necrosis, indicating that $FePS_3$-PEG nanosheets do not result in photothermal ablation effect without 808-nm laser. However, there is a marked contrast from Fig. 6d that tumor tissues are mostly damaged in G4 and the tumor growth is significantly suppressed with $FePS_3$-PEG nanosheets under 808-nm laser.

In order to evaluate the photothermal therapeutic effect of $FePS_3$-PEG nanosheets *in vivo*, we also measured the changes of tumor volume and weight of mice after photothermal treatments. It can be observed from Fig. 7a that the tumors of mice treated with both $FePS_3$-PEG nanosheets and 808-nm laser are completely ablated after 21 day, while the tumor volumes of mice treated without $FePS_3$-PEG nanosheets or 808-nm laser increase up to 15-fold their initial size. Compared with the weight of excised tumor from control groups, that from the mice treated with both $FePS_3$-PEG nanosheets and 808-nm laser can be neglected (Fig. S9), indicating the efficient photothermal ablation of tumors by $FePS_3$-PEG nanosheets. The slightly increase of body weight of the mice in the course of PTT (Fig. 7b) suggests no side effect of $FePS_3$-PEG nanosheets. The photographs of the 4T1 tumor-bearing mice at various times after different

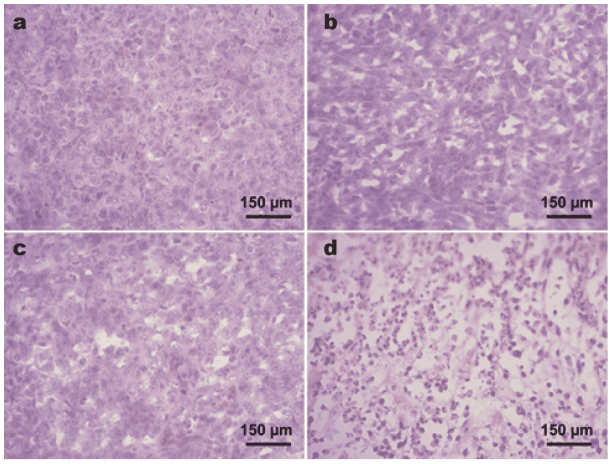

Figure 6 H&E staining of tumor tissues obtained from the mice in different treatment groups: (a) G1, (b) G2, (c) G3 and (d) G4.

treatments (Fig. 7c and Fig. S10) clearly present the photothermal therapeutic effect of $FePS_3$-PEG nanosheets under 808-nm laser. The biocompatibility of $FePS_3$-PEG nanosheets *in vivo* was also evaluated for their practical biomedical applications. The blood routines of mice after

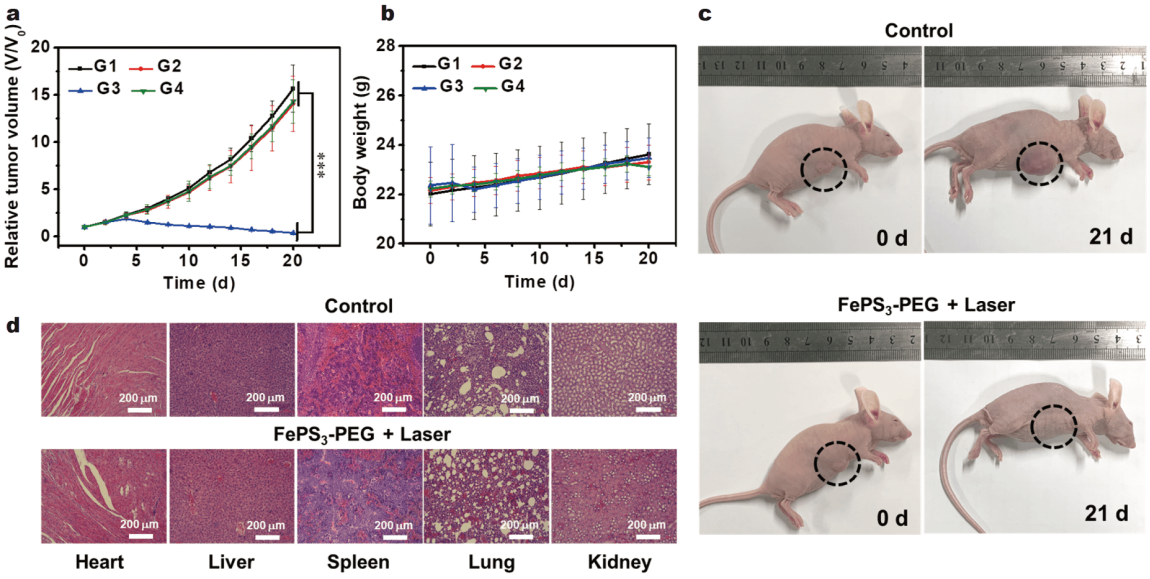

Figure 7 (a) Tumor growth curves along with time (Mean ± standard deviation (SD); $n = 5$ ($^{***}p < 0.001$, analyzed by one-way analysis of variance (ANOVA))). (b) Body weights of mice after various treatments. (c) The photographs of the mice without treatment (Control) or with the treatment of both $FePS_3$-PEG nanosheets and 808-nm laser ($FePS_3$-PEG + Laser). (d) Histological images of major organs from the mice without treatment (Control) or with the treatment of both $FePS_3$-PEG nanosheets and 808-nm laser ($FePS_3$-PEG + Laser). Concentration of $FePS_3$-PEG nanosheets: 300 μg mL^{-1}. Relative tumor volume (V/V_0) refers to the ratio of the tumor volume at the concerned time after treatment (V) to the initial tumor volume (V_0).

different treatments were measured to evaluate the risk factor for PTT of 4T1 tumor-bearing mice. It can be observed from Table S1 that there are no statistically significant differences in the results of blood routine among the 4 groups (G1, G2, G3 and G4), suggesting the high safety of PTT with $FePS_3$-PEG nanosheets. Furthermore, histological images in Fig. 7d show no inflammatory lesion and obvious damage for major organs of mice treated with both $FePS_3$-PEG nanosheets and 808-nm laser for 21 d, proving that there are no side effects and tumor metastasis for the use of $FePS_3$-PEG nanosheets in NIR PTT. All the experimental results demonstrate that $FePS_3$-PEG nanosheets have good biocompatibility and prominent NIR photothermal therapeutic effect for tumors under the guidance of T_1-MRI.

CONCLUSIONS

In summary, biocompatible thin-layered $FePS_3$-PEG nanosheets are synthesized by directly ultrasonic exfoliation and *in situ* chemical functionalization with PEG-NH_2. The resultant $FePS_3$-PEG nanosheets show excellent NIR photothermal properties with a high PCE (22.1%) and good photothermal stability. What's more, $FePS_3$-PEG nanosheets display evident T_1 relaxation (r_1 = 2.69 $(mmol\ L^{-1})^{-1}\ S^{-1}$) in external magnetic fields and is promising to replace commercial Gd-based T_1-MRI contrast agents, which dominate T_1-MRI clinical applications. The experimental results *in vivo* demonstrate that $FePS_3$-PEG nanosheets have high-contrast T_1-MRI and prominent NIR photothermal therapeutic effect on the 4T1 tumor-bearing mice. $FePS_3$-PEG nanosheets as a kind of bifunctional 2D nanomaterials are promising for T_1-MRI and NIR PTT in the biomedical applications.

Received 12 January 2021; accepted 2 February 2021; published online 27 April 2021

1 Seo WS, Lee JH, Sun X, *et al.* FeCo/graphitic-shell nanocrystals as advanced magnetic-resonance-imaging and near-infrared agents. Nat Mater, 2006, 5: 971–976
2 Jin Y, Jia C, Huang SW, *et al.* Multifunctional nanoparticles as coupled contrast agents. Nat Commun, 2010, 1: 41
3 Yu J, Yang C, Li J, *et al.* Multifunctional Fe_5C_2 nanoparticles: A targeted theranostic platform for magnetic resonance imaging and photoacoustic tomography-guided photothermal therapy. Adv Mater, 2014, 26: 4114–4120
4 Li B, Ye K, Zhang Y, *et al.* Photothermal theragnosis synergistic therapy based on bimetal sulphide nanocrystals rather than nanocomposites. Adv Mater, 2015, 27: 1339–1345
5 Tan C, Cao X, Wu XJ, *et al.* Recent advances in ultrathin two-dimensional nanomaterials. Chem Rev, 2017, 117: 6225–6331
6 Zhou Z, Li B, Shen C, *et al.* Metallic 1T phase enabling MoS_2 nanodots as an efficient agent for photoacoustic imaging guided photothermal therapy in the near-infrared-II window. Small, 2020, 16: 2004173
7 Zhou Z, Wang X, Zhang H, *et al.* Activating layered metal oxide

nanomaterials *via* structural engineering as biodegradable nanoagents for photothermal cancer therapy. Small, 2021, 17: 2007486
8 Chou SS, Kaehr B, Kim J, *et al.* Chemically exfoliated MoS_2 as near-infrared photothermal agents. Angew Chem Int Ed, 2013, 52: 4160–4164
9 Liu T, Wang C, Gu X, *et al.* Drug delivery with PEGylated MoS_2 nano-sheets for combined photothermal and chemotherapy of cancer. Adv Mater, 2014, 26: 3433–3440
10 Liu Y, Ji X, Liu J, *et al.* Tantalum sulfide nanosheets as a theranostic nanoplatform for computed tomography imaging-guided combinatorial chemo-photothermal therapy. Adv Funct Mater, 2017, 27: 1703261
11 Cheng L, Liu J, Gu X, *et al.* PEGylated WS_2 nanosheets as a multifunctional theranostic agent for *in vivo* dual-modal CT/photoacoustic imaging guided photothermal therapy. Adv Mater, 2014, 26: 1886–1893
12 Chen Y, Ye D, Wu M, *et al.* Break-up of two-dimensional MnO_2 nanosheets promotes ultrasensitive pH-triggered theranostics of cancer. Adv Mater, 2014, 26: 7019–7026
13 Yin W, Yan L, Yu J, *et al.* High-throughput synthesis of single-layer MoS_2 nanosheets as a near-infrared photothermal-triggered drug delivery for effective cancer therapy. ACS Nano, 2014, 8: 6922–6933
14 Du K, Wang X, Liu Y, *et al.* Weak van der Waals stacking, wide-range band gap, and Raman study on ultrathin layers of metal phosphorus trichalcogenides. ACS Nano, 2016, 10: 1738–1743
15 Wang F, Shifa TA, Yu P, *et al.* New frontiers on van der Waals layered metal phosphorous trichalcogenides. Adv Funct Mater, 2018, 28: 1802151
16 Chen Z, Zhang W, Yang Z. A review on cathode materials for advanced lithium ion batteries: Microstructure designs and performance regulations. Nanotechnology, 2020, 31: 012001
17 Wang X, Du K, Liu YYF, *et al.* Raman spectroscopy of atomically thin two-dimensional magnetic iron phosphorus trisulfide ($FePS_3$) crystals. 2D Mater, 2016, 3: 031009
18 Lee JU, Lee S, Ryoo JH, *et al.* Ising-type magnetic ordering in atomically thin $FePS_3$. Nano Lett, 2016, 16: 7433–7438
19 Gao Y, Lei S, Kang T, *et al.* Bias-switchable negative and positive photoconductivity in 2D $FePS_3$ ultraviolet photodetectors. Nanotechnology, 2018, 29: 244001
20 Cheng Z, Shifa TA, Wang F, *et al.* High-yield production of monolayer $FePS_3$ quantum sheets *via* chemical exfoliation for efficient photocatalytic hydrogen evolution. Adv Mater, 2018, 30: 1707433
21 Zhu W, Gan W, Muhammad Z, *et al.* Exfoliation of ultrathin $FePS_3$ layers as a promising electrocatalyst for the oxygen evolution reaction. Chem Commun, 2018, 54: 4481–4484
22 Liang Q, Zheng Y, Du C, *et al.* General and scalable solid-state synthesis of 2D MPS_3 (M = Fe, Co, Ni) nanosheets and tuning their Li/Na storage properties. Small Methods, 2017, 1: 1700304
23 Mukherjee D, Austeria PM, Sampath S. Two-dimensional, few-layer phosphochalcogenide, $FePS_3$: A new catalyst for electrochemical hydrogen evolution over wide pH range. ACS Energy Lett, 2016, 1: 367–372
24 Liu G, Guo W, Yin Z. Covalent fabrication of methyl parathion hydrolase on gold nanoparticles modified carbon substrates for designing a methyl parathion biosensor. Biosens Bioelectron, 2014, 53: 440–446
25 Manrıquez V, Barahona P, Peña O, *et al.* Physical properties of layer-type MPS_3 compounds: $M_{0.5}In_{0.33}PS_3$ (M=Cd, Fe, Mn). J Alloys Compd, 2001, 329: 92–96
26 Rastogi SK, Anderson HE, Lamas J, *et al.* Enhanced release of molecules upon ultraviolet (UV) light irradiation from photo-responsive hydrogels prepared from bifunctional azobenzene and four-arm poly(ethylene glycol). ACS Appl Mater Interfaces, 2018, 10: 30071–30080
27 Chen F, Yang D, Shen H, *et al.* Hydrothermal synthesis of novel rhombic dodecahedral SnS nanocrystals for highly efficient photothermal therapy. Chem Commun, 2019, 55: 2789–2792
28 Xie H, Li Z, Sun Z, *et al.* Metabolizable ultrathin Bi_2Se_3 nanosheets in imaging-guided photothermal therapy. Small, 2016, 12: 4136–4145
29 Yang K, Wan J, Zhang S, *et al.* The influence of surface chemistry and size of nanoscale graphene oxide on photothermal therapy of cancer using ultra-low laser power. Biomaterials, 2012, 33: 2206–2214
30 Jiang F, Ding B, Zhao Y, *et al.* Biocompatible CuO-decorated carbon nanoplatforms for multiplexed imaging and enhanced antitumor efficacy *via* combined photothermal therapy/chemodynamic therapy/chemotherapy. Sci China Mater, 2020, 63: 1818–1830
31 Zeng J, Goldfeld D, Xia Y. A plasmon-assisted optofluidic (PAOF) system for measuring the photothermal conversion efficiencies of gold nanostructures and controlling an electrical switch. Angew Chem, 2013, 125: 4263–4267
32 An L, Cai Y, Tian Q, *et al.* Ultrasensitive iron-based magnetic resonance contrast agent constructed with natural polyphenol tannic acid for tumor theranostics. Sci China Mater, 2021, 64: 498–509
33 Na H, Lee J, An K, *et al.* Development of a T_1 contrast agent for magnetic resonance imaging using MnO nanoparticles. Angew Chem, 2007, 119: 5493–5497
34 Im GH, Kim SM, Lee DG, *et al.* Fe_3O_4/MnO hybrid nanocrystals as a dual contrast agent for both T_1- and T_2-weighted liver MRI. Biomaterials, 2013, 34: 2069–2076
35 Wei H, Bruns OT, Kaul MG, *et al.* Exceedingly small iron oxide nanoparticles as positive MRI contrast agents. Proc Natl Acad Sci USA, 2017, 114: 2325–2330
36 Chen B, Guo Z, Guo C, *et al.* Moderate cooling coprecipitation for extremely small iron oxide as a pH dependent T_1-MRI contrast agent. Nanoscale, 2020, 12: 5521–5532
37 Yang W, Guo W, Le W, *et al.* Albumin-bioinspired Gd:CuS nanotheranostic agent for *in vivo* photoacoustic/magnetic resonance imaging-guided tumor-targeted photothermal therapy. ACS Nano, 2016, 10: 10245–10257

Acknowledgements This work was supported by the National Key Research and Development Program of China (2017YFA0205302), the Key Grant for Special Professors in Jiangsu Province (RK030STP18001), the Key Research and Development Program of Jiangsu (BE2018732), the Natural Science Key Fund for Colleges and Universities in Jiangsu Province (17KJA430011), the National Postdoctoral Program for Innovative Talents (BX20190156), the Scientific Research Foundation of Nanjing University of Posts and Telecommunications (NY218150), the Training Program of the Major Research Plan of the National Natural Science Foundation of China from Nanjing University of Posts and Telecommunications (NY218158), "1311 Talents Program" of Nanjing University of Posts and Telecommunications, "100 Top Talents Program" of Sun Yat-sen University (29000-18841216), "Young-Teacher

Training Program" of Sun Yat-sen University (29000-31610036), Joint Funds for the Innovation of Science and Technology in Fujian Province (2017Y9111), and the Natural Science Foundation of Fujian Province (2020J01613).

Author contributions Zhang Y designed the experiments and wrote the draft of manuscript. Du H, He P, Shen C and Li Q prepared the $FePS_3$-PEG nanosheets and characterized them. Duan Y, Shao Z, Mu F and Huang F designed and carried out the biological experiments. Li P, Gao P and Yu P provided suggestions and comments on the manuscript. Luo Z and Wang L proposed the project and revised the manuscript.

Conflict of interest The authors declare that they have no conflict of interest.

Supplementary information Experimental details and supporting data are available in the online version of the paper.

Ying Zhang obtained her PhD degree in bioelectronics from Nanjing University of Posts and Telecommunications (NJUPT) in 2016. She is now an associate professor at the College of Electronic and Optical Engineering & College of Microelectronic, NJUPT. Her research interests focus on biosensing and phototheranostics based on novel optoelectronic nanomaterials.

Feng Huang obtained his PhD degree in development biology from Fujian Normal University in 2015. He is now a lecture of Fujian Medical University. His current research interests include biological characteristics of nanomaterials and nanotechnology in diagnosis and treatment of tumors.

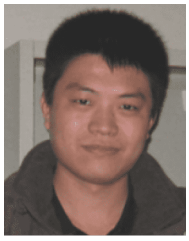

Peng Yu obtained his PhD degree from the University of Chinese Academy of Sciences in 2013, and was a research fellow in the research group of Professor Zheng Liu at Nanyang Technological University from 2014 to 2018. He is now an associate professor of "100 Top Talents Program" at Sun Yat-sen University. His research interests focus on nonlinear optical materials, high-performance electronic devices, and optoelectronic devices.

Zhimin Luo obtained his PhD degree in polymeric chemistry and physics at Fudan University under the supervision of Prof. Lianhui Wang in 2013, and worked as a research fellow in Prof. Hua Zhang's group at Nanyang Technological University in Singapore from 2013 to 2018. He is now a professor at the Institute of Advanced Materials, NJUPT. He was honored as "Special Professors in Jiangsu Province". His research interests focus on the synthesis of novel optoelectronic nanomaterials for biological and electrochemical applications.

Lianhui Wang obtained his PhD degree in polymeric chemistry and physics at Zhejiang University in 1998, and was a research fellow in Prof. E. T. Kang's group at the National University of Singapore (NUS) from 1998 to 2000, followed by being an assistant professor at the Institute of Molecular and Cell Biology, NUS. Since June 2005, he joined the faculty of Fudan University as a professor and then moved to NJUPT in January 2011. Currently, he is a professor at the Institute of Advanced Materials, NJUPT. He was granted the funding of "National Distinguished Young Scholar" in 2004, and was honored as "Yangtze River Scholar Distinguished Professor" in 2011. His research group works on bioelectronics and nanobiology including the synthesis of optoelectronic nanomaterials and their applications for biochemical sensing, multimodal imaging, drug delivery and photothermo/chemo/photodynamic therapy.

剥离的$FePS_3$纳米片及其活体内T_1加权磁共振成像介导的近红外光热治疗研究

张颖[1], 都洪芳[1], 何盼盼[1], 沈闯[1], 李琦[1], 段叶凡[1], 邵周伟[1], 牟菲[1], 黄峰[3*], 李霈旸[2], 高平齐[2], 于鹏[2*], 罗志敏[1*], 汪联辉[1*]

摘要 开发具有先进生物成像和高性能诊疗功能的纳米平台对于纳米科学与生物医药研究有重要意义. 本文中, 我们通过在氩气中超声剥离$FePS_3$单晶并同步化学修饰氨基聚乙二醇制备了氨基聚乙二醇功能化的$FePS_3$纳米片($FePS_3$-PEG), $FePS_3$-PEG纳米片在808 nm激光下的光热转化效率可达22.1%, 并在外界磁场中显示了明显的T_1弛豫效应(r_1 = 2.69 (mmol L^{-1})$^{-1}$ S^{-1}). 体内外的生物实验结果表明, $FePS_3$-PEG纳米片具有良好的生物相容性, 在清晰的T_1加权磁成像介导下展现出优异的光热治疗效果. $FePS_3$-PEG纳米片的特性使其成为有前景的癌症T_1加权磁成像介导的近红外光热治疗纳米药物.

